Quantum nanophotonic interface for tin-vacancy centers in thin-film diamond

Hope Lee,[1,*] Hannah C. Kleidermacher,[1,*] Abigail J.M. Stein,[1,*] Hyunseok Oh,[2] Lillian B. Hughes Wyatt,[3] Casey K. Kim,[3] Luca Basso,[4] Andrew M. Mounce,[4] Yongqiang Wang,[5] Shei S. Su,[4] Michael Titze,[4,6] Ania C. Bleszynski Jayich,[2] and Jelena Vučković[1,†]

[1] *Edward L. Ginzton Lab, Stanford University, Stanford, California 94305, USA*
[2] *Department of Physics, University of California, Santa Barbara, California 93106, USA*
[3] *Materials Department, University of California, Santa Barbara, California 93106, USA*
[4] *Sandia National Laboratories, Albuquerque, New Mexico 87123, USA*
[5] *Los Alamos National Laboratory, Los Alamos, New Mexico 87545, USA*
[6] *Advanced Instrumentation for Nano-Analytics, Luxembourg Institute of Science and Technology, Belvaux L-4422, Luxembourg*

(Received 9 November 2025; revised 26 January 2026; accepted 13 March 2026; published 27 April 2026)

The negatively charged tin-vacancy center in diamond (SnV^-) is an excellent solid-state qubit with optically addressable transitions and a long electron spin-coherence time at elevated temperatures (approximately 1.7 K). However, implementing scalable quantum nodes with high-fidelity optical readout of the electron spin state requires efficient photon emission and collection from the system. In this manuscript, we report a quantum photonic interface for SnV^- centers based on one-dimensional photonic crystal cavities fabricated in diamond thin films. Furthermore, we provide a rigorous description of the spontaneous emission dynamics of our system, taking into account individual contributions from both the C and D transitions of the emitter. This allows for the determination of Purcell factors per transition and, by extension, the C/D branching ratio SnV^- zero-phonon line. We observe quality factors of up to approximately 6000 across this sample, and we measure up to a 12-fold lifetime reduction, which translates into a Purcell factor of $F_C = 26.2 \pm 1.5$ for a targeted C transition. By considering the cavity-mode polarization alignment with the C- and D-transition dipole moments, we validate the C/D branching ratio to be $\eta_{BR} = 0.75 \pm 0.01$, in line with previous theoretical and experimental findings.

DOI: 10.1103/vwt7-b64x

I. INTRODUCTION

Optically active defects in semiconductors, or color centers, are a leading platform for quantum network qubits due to their long spin-coherence times, bright optical emission, and native compatibility with nanophotonic integration [1–3]. Although the initial keystone quantum network demonstrations used the nitrogen vacancy (NV^-) center in diamond [4,5], negatively charged group-IV color centers in diamond have garnered interest due to their first-order insensitivity to electric-field noise and increased fraction of coherent emission into the zero-phonon line (ZPL) [6]. These features render the group-IV vacancy centers significantly more compatible with nanophotonic integration, which is required for downstream scaling of multiple quantum network nodes. The most established of the group-IV vacancies is the negatively charged silicon vacancy center (SiV^-), which has enabled long-distance networking demonstrations on the scale of those achieved with NV^- centers [7]. However, the SiV^- suffers from a limited ground-state splitting of approximately 50 GHz, necessitating either millikelvin dilution-refrigerator environments or diligent strain engineering for spin-state control. In contrast, the rapidly maturing tin vacancy (SnV^-) maintains spin coherence at liquid-helium temperatures, around 1.7 K, due to its significantly larger ground-state splitting of approximately 850 GHz [8,9].

The tin vacancy has similarly demonstrated its suitability as a qubit for long-distance quantum networks with high-fidelity initialization, manipulation, and readout of the qubit spin states and coupling to nanophotonic devices [9–16]. However, photonic interfaces for the SnV^- have thus far been fabricated via diamond bulk-carving techniques [17,18], severely limiting device performance, fabrication yield, and the feasibility of on-chip integration with other photonic and electronic components. Thus, the adoption of thin-film diamond paves the way for scalable quantum networks [19–21].

*These authors contributed equally to this work.
†Contact author: jela@stanford.edu

In this manuscript, we report the fabrication of one-dimensional (1D) photonic crystal cavities with quality factors of up to approximately 6000. In particular, we fabricated two orientations of cavity devices, one parallel to and one at approximately 55° to the ⟨100⟩ axis of the diamond lattice. For each cavity orientation ("parallel" and "angled"), we measure the lifetime reduction of two ZPL transitions (C and D) of a SnV^- color center. These transitions have the same spatial positioning in the cavity field but orthogonally polarized dipole moments. The ratio of the C to D transition emission rates is referred to as the branching ratio (η_{BR}) [6,18,22]. The conventional figure of merit for color center–cavity coupling is the Purcell factor, defined as the enhancement in spontaneous emission rate for a particular transition when on resonance with the cavity mode.

For previous reports of SnV^- coupling to photonic crystal cavities, Purcell factors were often calculated by applying multiplicative correction factors to the measured lifetime-reduction ratio without individual consideration of the C/D transitions and their distinct angular orientations [12,17]. To perform a more rigorous treatment, we construct a model to describe the spontaneous emission dynamics of our system and take into account both the C and D transitions, in line with the analysis presented in Ref. [23,24]. Using this model, we report a Purcell factor of up to $F_C = 26.2 \pm 1.5$ for the C transition in the angled device, for which the cavity-mode polarization and transition dipole moment are best aligned out of the available combinations. Furthermore, we numerically validate the C/D transition branching ratio to be $\eta_{BR} \approx 0.75 \pm 0.01$, in agreement with previous reports [6,18,22], and we estimate a global lithographic angular offset of $\delta\psi \approx 8.51°$. These results constitute crucial progress toward the implementation of scalable quantum networks based on the SnV^-.

II. RESULTS

A. Device design and fabrication

Thin-film diamond was prepared via the procedures outlined in Ref. [20]. Sn^{2+} was implanted into the bulk sample prior to membrane exfoliation with an implantation energy of 380 keV and at a dose of 2×10^{11} ions/cm^2, targeting SnV^- formation approximately 90 nm below the surface. Final membrane thicknesses were tuned to 180 nm by reactive-ion etching. Further details on thin-film preparation are provided in Appendix A 1.

Photonic crystal cavities were designed with a 300-nm beam width and 115-nm-diameter holes etched into the diamond film. The mirror reflectors consist of 10 holes on each side, while the central cavity consists of 12 holes, with quadratically tapered lattice spacings. To account for fabrication infidelities and ensure resonances in proximity to the SnV^- 619-nm ZPL wavelength, we sweep the lattice spacings from 180 to 210 nm in steps of 2.5 nm per device.

For the cavities reported in this manuscript, we measure a postfabrication beam width of 326 ± 13 nm, an average hole diameter of 134 ± 3 nm, and a lattice constant of 210 nm for the parallel device; and a beam width of 325 ± 2 nm, an average hole diameter of 119 ± 4 nm, and a lattice constant of 197.5 nm for the angled device, determined via scanning electron microscopy [Fig. 1(b)]. We note that our etch recipe renders a sidewall angle of approximately 5–10°. Taking these dimensions into account, we simulate quality factors (Q) of 2.8×10^5 (2.3×10^4) and mode volume (V) 0.46 (0.46) $(\lambda/n)^3$ for the parallel (angled) device. Further discussion of device design and fabrication yield is provided in Appendices A 2 and A 3. To optimize the use of the limited diamond film, transmission access to the cavities (e.g., via grating couplers or adiabatic tapers) was forgone, and instead all devices were probed confocally out of plane.

B. Characterization of devices and color centers

Throughout the measurements, the sample is maintained at 4 K in a Montana Instruments closed cycle cryostat. We use two discrete optical paths, subsequently referred to as the (i) cross-polarized and (ii) photoluminescence (PL) paths. These two optical paths enable independent access to the cavity resonance and color center signals.

We start by probing our cavity resonances using the cross-polarized reflectivity path. The cavities are mounted such that the resonance modes for parallel devices are primarily vertically polarized. Devices are excited confocally via a broadband supercontinuum laser, and the reflected signal is collected confocally and detected by a spectrometer. The excitation and collection paths are mixed via a polarizing beam splitter (PBS), and a half-wave plate (HWP) is inserted in the shared path right before the cryostat. The HWP is rotated to either approximately 45° or approximately 100° to optimize the resonance signal-to-noise ratio (SNR) of the parallel and angled devices, respectively. Further detail on the optical setup is provided in Appendix B.

Each broadband reflectivity spectrum is background corrected and then fitted to a Fano model. For the parallel device, we determine a quality factor of 6032 [Fig. 1(c)]. The quality factor of the angled device was determined to be 3942, as discussed in Appendix D 2. We note that this method of fitting a Fano model to the spectral features in reflectivity serves as a lower-bound estimator for the quality factors. Further discussion is provided in Appendix D 3.

1. PL enhancement

Next, we perform PL spectroscopy to identify emitters located in the cavity mode, exciting with approximately

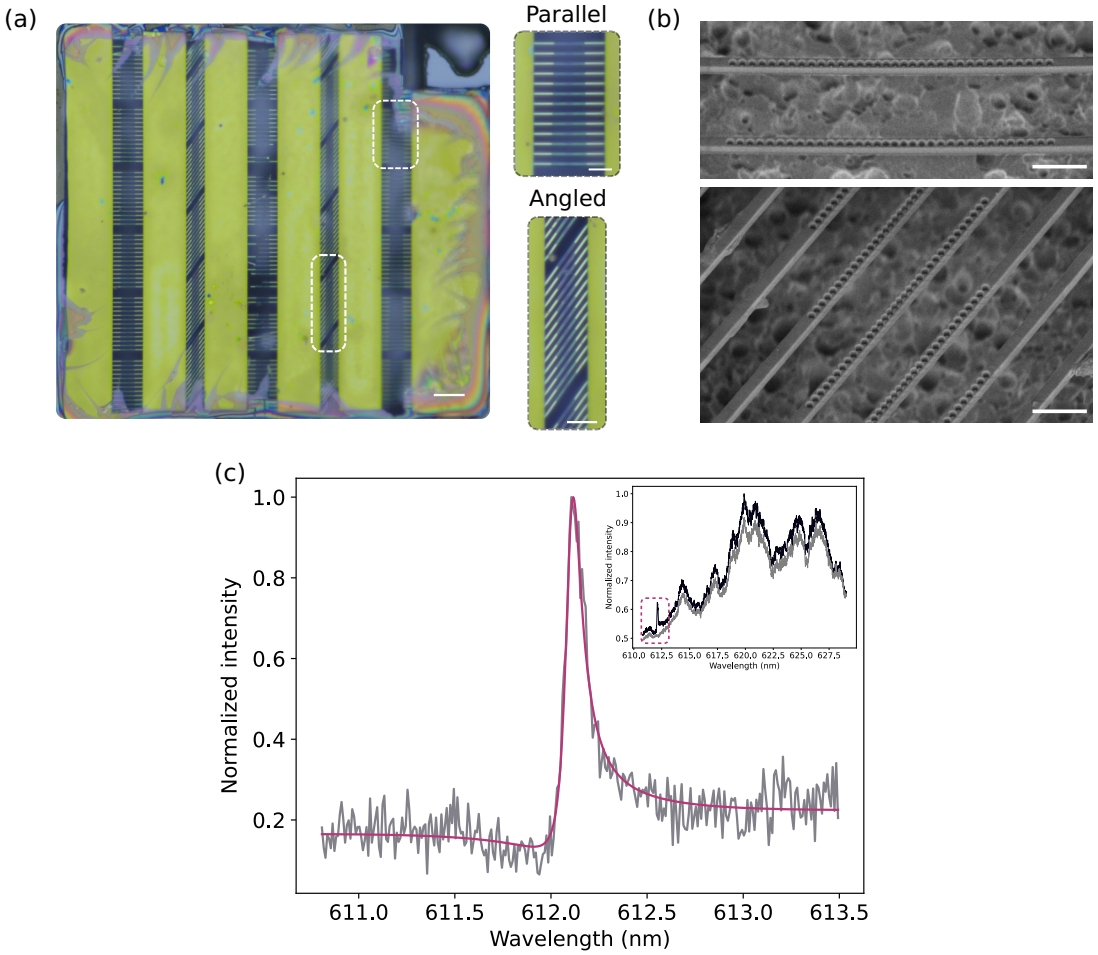

FIG. 1. Cavity design, fabrication, and characterization. (a) A white-light image of the fabricated devices on the thin-film membrane. Representations of the two classes of devices, parallel and angled, are indicated by the white dashed boxes and enlarged to be shown in greater detail. The scale bars indicate 15 and 5 μm for the overview and enlarged images, respectively. (b) Scanning electron microscope image of fabricated devices. Scale bars indicate 1 μm. (c) Cross-polarized reflectivity spectrum for the parallel device. The broadband spectrum is background corrected and then fitted to a Fano model, yielding a quality factor of 6032. The inset shows the broadband reflectivity spectra for both the resonance and the background. The fitted region is indicated by the dashed box. In the inset, the background spectrum is represented by the lighter, gray data trace, and the reflectivity spectrum is shown by the darker trace.

5 mW of a 520-nm continuous-wave (CW) source and filtering collected counts with a 620/14-nm bandpass filter [Fig. 2(b)]. Due to the high implantation density, approximately two to three emitters lie within our cavity mode. To probe for emitter-cavity coupling, we first redshift the cavity resonance past the identified SnV^- transitions via argon-gas condensation. Then, we "back-tune" the resonance controllably by illuminating the nanobeam with approximately 0.75 mW of green excitation power to evaporate condensed gas while simultaneously collecting PL spectra to characterize SnV^- PL enhancement [Fig. 2(c)]. For the parallel device, we identify an approximately tenfold PL enhancement of the emitter when the cavity is tuned into resonance with the transition [Fig. 2(d)]. This measure of PL enhancement indicates significant emitter-cavity coupling, but it does not suffice as an accurate measure of the Purcell factor given uncertainties in exact collection efficiencies. PL enhancement measurements for the angled device are provided in Appendix D 2.

2. Lifetime reduction

To quantify Purcell factors, we measure the lifetime reduction of the emitter when the cavity is tuned into resonance. As before, we red-detune the cavity resonance beyond the SnV^- transition in preparation to back-tune across the target wavelength; however, we now toggle our excitation between the cross-polarized path, which is used to both monitor and back-tune the resonance wavelength, and the PL path, which is used to measure the emitter optical lifetime. In the cross-polarized path, we excite simultaneously with both the supercontinuum and

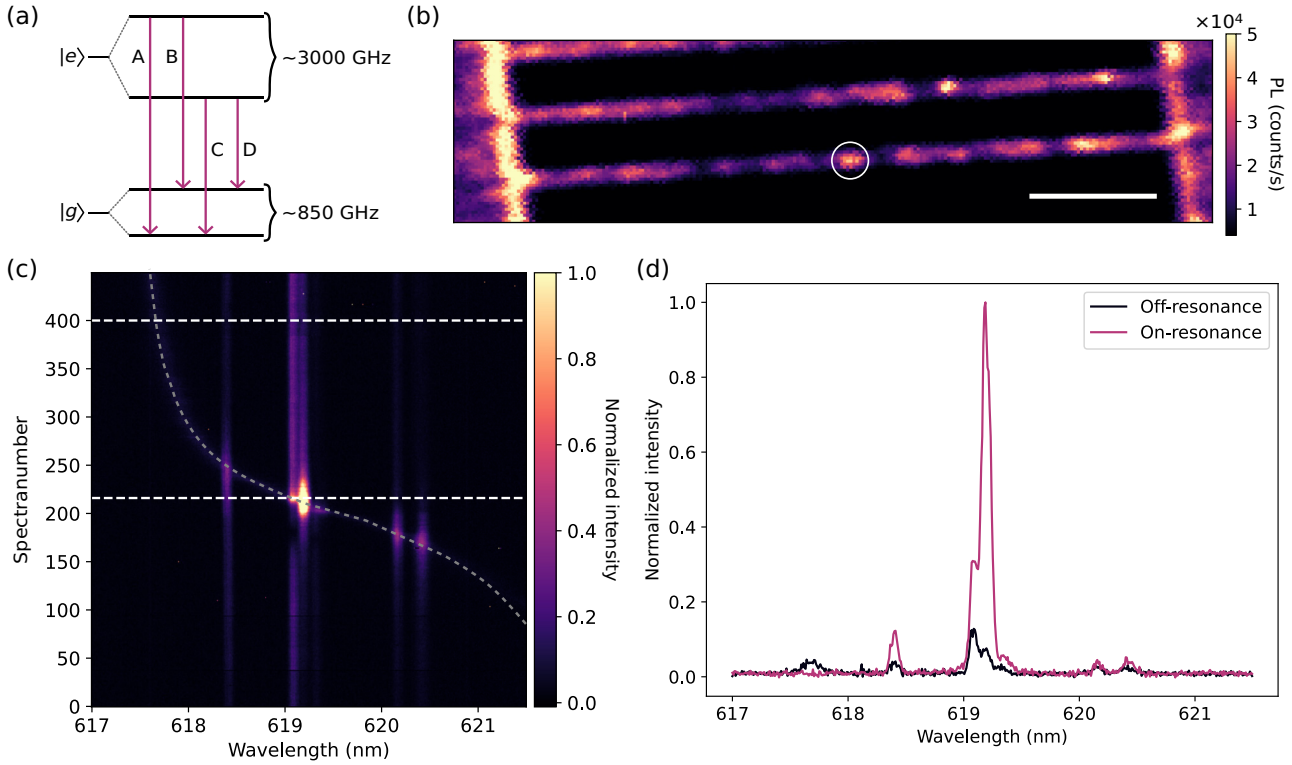

FIG. 2. Level structure of SnV^-, PL confocal scan and cavity enhancement. (a) Schematic of the orbital energy states of the SnV^-. Characteristic of a group-IV color center, the ground ($|g\rangle$) and excited states ($|e\rangle$) are each split via the combined effects of spin-orbit coupling and the Jahn-Teller effect. For the SnV^-, the ground-state splitting is approximately 850 GHz and the excited-state splitting approximately 3000 GHz; these state splittings yield four separate ZPL transitions. In cryogenic conditions, the PL signal is dominated by the two longer-wavelength, lower-energy transitions, labeled as C and D [25]. (b) PL confocal scan of the parallel device. The emitter cluster addressed is indicated by the white circle. The scale bar indicates 3 μm. (c) PL enhancement via gas tuning. The cavity resonance is first redshifted via Ar gas condensation past all SnV^- transitions of interest. The sample is then naturally "back-tuned" over the course of repeated PL spectra. The two spectra of interest are indicated by the white dashed lines. The gray dashed line is an approximate guide for the eye of the cavity resonance. (d) PL spectra on and off resonance with the cavity. We see that the most strongly enhanced SnV^- transition demonstrates an approximately tenfold PL enhancement.

the CW green diode laser (set again to approximately 0.75 mW) to both monitor and back-tune the cavity resonance. In the PL path, we isolate a single transition with a narrowband (approximately 0.3 nm) tunable filter and excite the emitter above band with a 520-nm pulsed laser. We apply excitation pulses with 16-ns pulse widths, a 3.3-MHz repetition rate, and an averaged power of 270 μW. Each lifetime trace is integrated for 3 min to build up suitable count rates, while each cross-polarized resonance spectrum is integrated for 3 s to allow ample time for the cavity resonance to gradually back-tune across the transition.

We target selective collection from the C transition, but due to the C and D transitions sharing an excited state, we see significant lifetime reduction when the cavity is on resonance with either transition individually. Furthermore, we will show in Sec. II B 3 that by considering the orthogonality of the C and D dipoles, we can extract individual Purcell factors for each transition, and by extension, the C/D branching ratio. In preparation for this analysis, we calculate the spontaneous emission rate from the measured emitter decay lifetime via $\Gamma = 1/\tau_{\text{lifetime}}$. When resonant with the cavity, transition C (D) demonstrates a lifetime of 1.85 ± 0.02 ns or an emission rate of 0.54 ns^{-1} (4.57 ± 0.02 ns or an emission rate of 0.22 ns^{-1}) compared to the off-resonance lifetime of 9.41 ± 0.09 ns or an emission rate of 0.11 ns^{-1} [Fig. 3(c)]. We then fit the data to the sum of two Lorentzians. Dividing a fitted Lorentzian peak by the background yields an emission-rate enhancement ratio, which we denote as ζ. For the C and D transitions, we extract $\zeta_C = 4.67 \pm 0.07$ and $\zeta_D = 1.99 \pm 0.02$, respectively [Fig. 3(a)].

For the angled device, there remain contributions from a secondary emitter in the collected counts. We therefore fit the spontaneous emission rates to the sum of four Lorentzians but focus our analysis on the more prominent emitter. We determine that transition C (D) demonstrates a lifetime of 1.08 ± 0.01 ns or an emission rate 0.93 1/ns (8.11 ± 0.23 ns or an emission rate of 0.12 ns^{-1}) compared to the off-resonance lifetime of 10.51 ± 0.19 ns or an

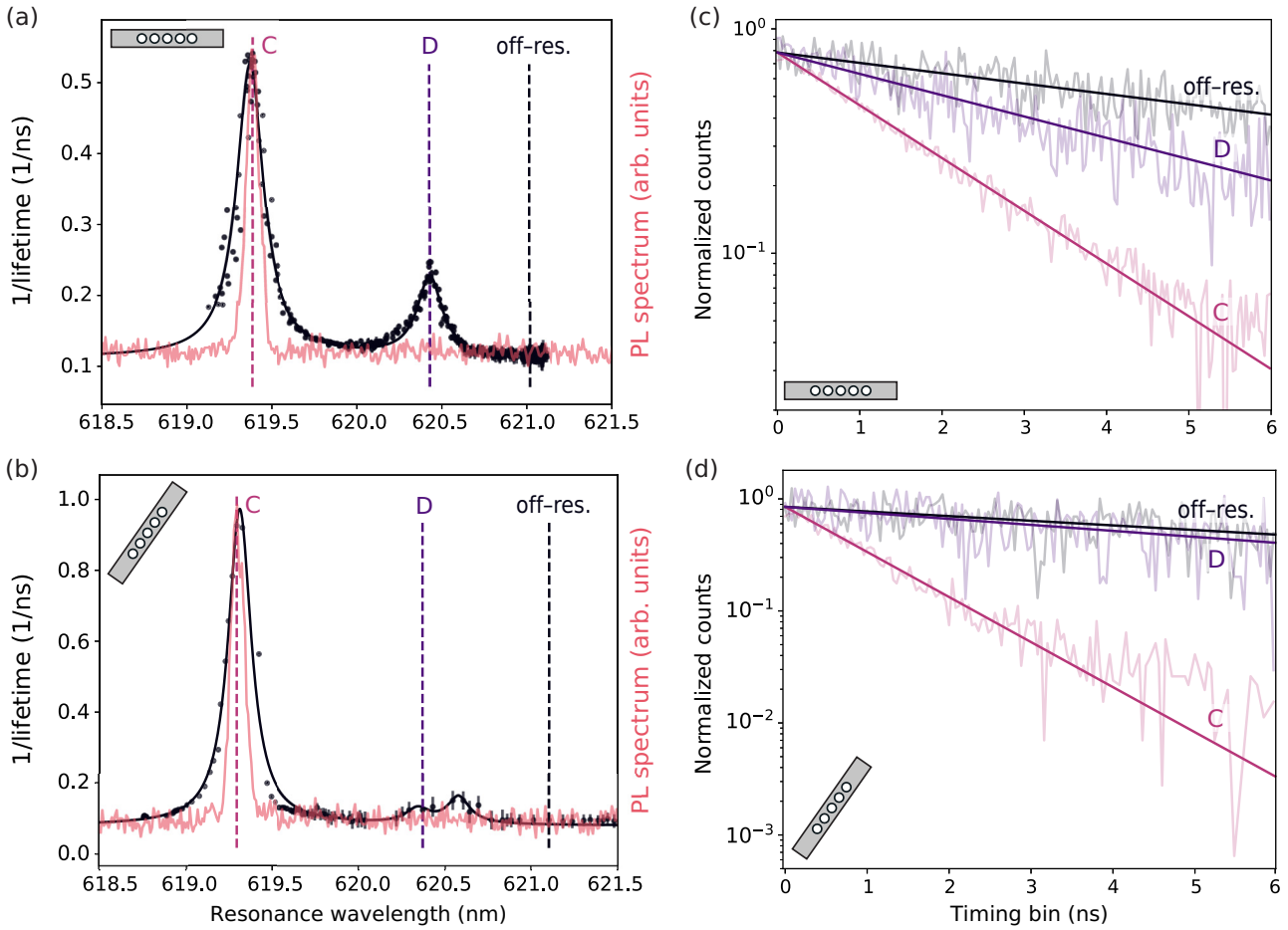

FIG. 3. Lifetime-reduction and branching ratio analysis. (a) Spontaneous emission rate vs cavity resonance wavelength for the parallel device (black). The data are fitted to a model consisting of the sum of two Lorentzians. The PL spectrum (red) is overlaid. We extract the amplitude ratios $\zeta_C = 4.672$ and $\zeta_D = 1.985$ from this fit model. The three vertical dashed lines indicate the lifetime slices that are plotted separately, representing the traces with the C transition on resonance (pink), the D transition on resonance (purple), and both transitions off resonance (black). (b) Spontaneous emission rate vs cavity resonance wavelength for the angled device (black). As in (a), the PL spectrum (red) is overlaid. For this device, we extract the amplitude ratios $\zeta_C = 12.230$ and $\zeta_D = 1.514$ from this fit model. We note that due to filtering limitations, there are contributions from two separate emitters, and the data are thus fitted to the sum of four Lorentzians. The dashed lines indicate the lifetime slices of interest, as in panel (a). (c) Normalized lifetimes of the SnV^- with C and D transitions on and off resonance for the parallel device. We measure an off-resonance lifetime of 9.412 ± 0.09 ns. When the C (D) transition is on resonance with the cavity, the lifetime is reduced to 1.847 ± 0.002 ns (4.570 ± 0.02 ns). The lifetimes are fitted to amplitude-normalized and background-corrected single exponential models. (d) Normalized lifetimes of the SnV^- with C and D transitions on and off resonance for the angled device. We measure an off-resonance lifetime of 10.507 ± 0.2 ns. When the C (D) transition is on resonance, the lifetime is reduced to 1.079 ± 0.002 ns (8.109 ± 0.2 ns). The lifetimes are fitted to amplitude-normalized and background-corrected single exponential models. Due to the contributions of a second emitter transition, at longer timescales, the data begin to deviate slightly from a single exponential model; however, within the fitting range, the observed fluorescence lifetime is primarily dominated by a single decay timescale.

emission rate of 0.10 ns^{-1} [Fig. 3(d)]. The fitted amplitude ratios are $\zeta_C = 12.23 \pm 0.69$ and $\zeta_D = 1.51 \pm 0.27$ [Fig. 3(b)].

3. Purcell factors

Although our time-resolved fluorescence measurements are spectrally filtered to collect signal only from the C transition, the observed spontaneous emission rate reflects the dynamics of the excited-state population. The excited-state population can decay via either the C/D ZPL transitions or the phonon side band (PSB) and, consequently, the C-transition emission rate is enhanced when the cavity is tuned in resonance with either transition. This therefore motivates a rate-equation treatment to precisely extract the Purcell enhancement of each individual ZPL

transition, consistent in construction with that presented in Ref. [23,24].

We express the spontaneous emission dynamics of the full cavity-emitter system with the following expressions for spontaneous emission rates:

$$\Gamma_0 = \Gamma_C + \Gamma_D + \gamma_{PSB}, \tag{1}$$

$$\Gamma_{coupled} = F_C * \Gamma_C + F_D * \Gamma_D + \gamma_{PSB}, \tag{2}$$

where Γ_0 is the uncoupled or bulk emission rate and $\Gamma_{coupled}$ is the cavity-coupled enhanced spontaneous emission rate. In our analysis, we neglect contributions from the A/B ZPL transitions of the SnV^-, as the two higher-energy transitions are suppressed in cryogenic conditions [8]. Therefore, in the uncoupled case, the total spontaneous emission rate is given by the sum of Γ_C, the C-transition emission rate, Γ_D, the D-transition emission rate, and γ_{PSB}, the rate of emission into the PSB. In the cavity-coupled case, F_C and F_D represent the Purcell factor that enhances the emission into the two orthogonal ZPL transitions.

Dividing $\Gamma_{coupled}$ by Γ_0 to analyze the emission-enhancement ratios, we write

$$\begin{aligned}\zeta = \frac{\Gamma_{coupled}}{\Gamma_0} &= F_C * \frac{\Gamma_C}{\Gamma_0} + F_D * \frac{\Gamma_D}{\Gamma_0} + \frac{\gamma_{PSB}}{\Gamma_0} \\ &= F_C * \eta_{DW}\eta_{BR} \\ &\quad + F_D * \eta_{DW}(1-\eta_{BR}) + (1-\eta_{DW}),\end{aligned} \tag{3}$$

where $\eta_{DW} = 0.57$ is the Debye-Waller factor, or the coherent ZPL proportion of the total radiative emission [25]. Here, η_{BR} is the branching ratio between transitions C and D. We are able to write two separate ratios, ζ_C and ζ_D, for when the cavity is on resonance with transitions C and D, respectively. For the ratio ζ_C (ζ_D), we can set F_D (F_C) equal to 1.

We now recast these equations to solve for the Purcell factors:

$$F_C = 1 + \frac{\zeta_C - 1}{\eta_{DW}\eta_{BR}}, \tag{4}$$

$$F_D = 1 + \frac{\zeta_D - 1}{\eta_{DW}(1-\eta_{BR})}. \tag{5}$$

By formulating transition-specific rate equations, we avoid relying on "lump-sum" multiplicative correction factors or omitting explicit treatment of the individual C and D transitions [12,17].

Using the literature branching ratio value $\eta_{BR} = 0.78$ and the expressions derived above, we determine Purcell factors of $F_C = 26.2 \pm 1.5$ and $F_D = 5.1 \pm 2.2$ ($F_C = 9.2 \pm 0.2$ and $F_D = 8.9 \pm 0.1$) for the angled (parallel) cavity [6,18,22]. For the second emitter of the angled device, we can estimate Purcell factors of $F_C = 1.1 \pm 0.4$ and $F_D = 8.8 \pm 2.2$. We note that since the second emitter in the angled cavity demonstrates a larger Purcell factor for the D transition, we conclude that the emitter is oriented orthogonally to the other two emitters of study. Additional discussion regarding the second emitter is provided in Appendix D 1.

4. Cavity-mode polarization and emitter dipole moment angular alignment

We now extend the presented analysis to extracting the C/D branching ratio and cavity angular orientation and consider the relative orientation between the cavity-mode polarization and the C- and D-transition dipole moments. The dependence of the Purcell factor on the angular alignment between the emitter dipole moment and the cavity field is given by

$$F = F_o \frac{\left|\vec{\boldsymbol{\mu}} \cdot \vec{\mathbf{E}}(\mathbf{r})\right|^2}{\|\vec{\boldsymbol{\mu}}\|^2 \, \|\vec{\mathbf{E}}(\mathbf{r})\|^2}, \tag{6}$$

where $\vec{\boldsymbol{\mu}}$ is the dipole moment of the quantum emitter transition, $\vec{\mathbf{E}}(\mathbf{r})$ is the electric field at the position of the emitter, and F_o comprises all other contributions required to determine the Purcell factor (Q/V ratio, emitter spatial position, and spectral overlap between the emitter transition and cavity resonance wavelengths). In the case of a single SnV^- center, F_o therefore contains all multiplicative factors that are shared for the respective Purcell factors of the C and D transitions—the singular difference for the two transitions stems from the dipole moment-cavity field alignment. As such, we express F_C and F_D in the form

$$\begin{aligned}F_C &= F_o \left|\hat{\mathbf{C}} \cdot \hat{\mathbf{e}}_{cav}\right|^2, \\ F_D &= F_o \left|\hat{\mathbf{D}} \cdot \hat{\mathbf{e}}_{cav}\right|^2,\end{aligned} \tag{7}$$

where $\hat{\mathbf{C}}$ ($\hat{\mathbf{D}}$) is the unit dipole moment vector of the C (D) transition of a single SnV^- center and $\hat{\mathbf{e}}_{cav}$ is the unit polarization vector of the cavity mode. In a $\langle 100 \rangle$-oriented diamond, the C dipole possesses a substantial out-of-plane component, whereas the D dipole lies entirely in the sample plane (Fig. 4) [26]. This motivates the development of $\langle 111 \rangle$ diamond growth and devices, where crystallographic orientation is engineered to enable more favorable emitter-cavity alignment [15].

For the purposes of our analysis, we require all relevant vectors to be written in real-space coordinates. We therefore map the crystallographic dipole directions to real space as $\hat{x} \parallel \langle 100 \rangle$, $\hat{y} \parallel \langle 010 \rangle$, and $\hat{z} \parallel \langle 001 \rangle$ and write

$$\begin{aligned}\hat{\mathbf{C}} &= \langle \cos\phi \sin\theta, \sin\phi \sin\theta, \cos\theta \rangle, \\ \hat{\mathbf{D}} &= \langle \sin\phi, -\cos\phi, 0 \rangle, \\ \hat{\mathbf{e}}_{cav} &= \langle \sin\psi, \cos\psi, 0 \rangle,\end{aligned} \tag{8}$$

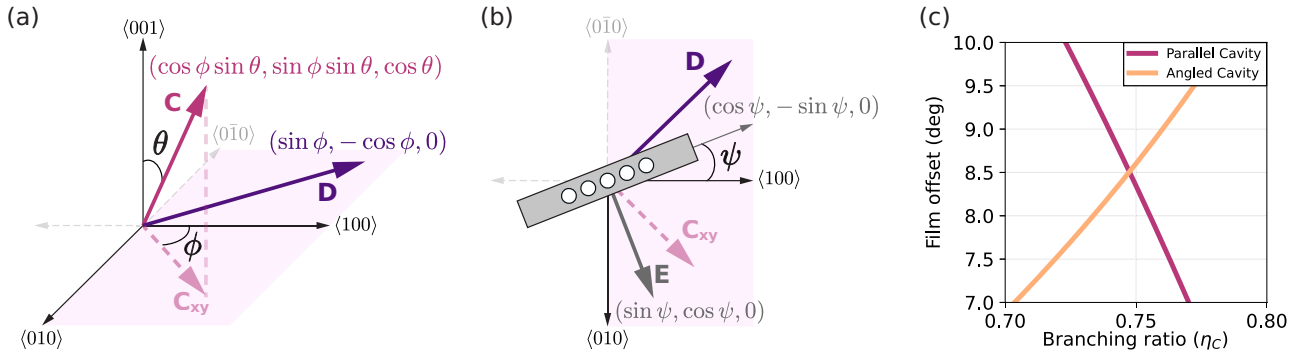

FIG. 4. Cavity-mode polarization and SnV^- transition dipole moment alignment. (a) Dipole orientations for a ⟨100⟩-oriented diamond. The C dipole points along lattice vector ⟨111⟩, giving a fixed out-of-plane tilt θ and an in-plane projection C_{xy}, with azimuthal angle ψ. The D dipole lies in plane along lattice vector ⟨1$\bar{1}$0⟩. For the purposes of the analysis, these dipole moment unit vectors are translated into real space and mapped onto the sample-fixed axes $\hat{x} \parallel \langle 100\rangle$, $\hat{y} \parallel \langle 010\rangle$, and $\hat{z} \parallel \langle 001\rangle$. The pink region denotes the sample surface plane. (b) Schematic of the sample surface and cavity orientation. The cavity is fabricated at an angle ψ relative to ⟨100⟩. The fundamental nanobeam mode polarization **E** is taken to be orthogonal to the cavity axis. The resulting polarization overlap with the transition dipole moments determines the Purcell enhancement of the C and D transitions. The pink region denotes the sample surface plane. (c) Solution of the analysis in Sec. II B 2 in allowing both η_{BR} and $\delta\phi$ to vary freely. We determine a branching ratio $\eta_{BR} \approx 0.75 \pm 0.01$ and fabrication offset $\delta\psi \approx 8.51°$.

where ϕ and ψ are azimuthal angles and θ is a polar angle. For the SnV^- in ⟨100⟩ diamond, $\phi \approx 45°$ and $\theta \approx 55°$. Further, $\hat{D}$ is oriented orthogonal to $\hat{C}$ in projection to the xy plane, and the effective azimuthal angle is therefore $\phi' = \phi - 90°$. The expression for $\hat{D}$ as written in Eq. (8) is simplified by trigonometric identifies. Crystallographic miscut of the diamond during polishing (approximately 1°) has been neglected in this analysis. Here, ψ represents the angle of the cavity nanobeam, which is lithographically defined during fabrication. In our case, we aimed for $\psi \approx 0°$ for parallel devices and $\psi \approx 55°$ for angled devices. Note that $\hat{\mathbf{e}}_{cav}$ has an effective azimuthal angle of $\psi' = \psi + 90°$ as the electric-field polarization of the cavity mode is orthogonal to the nanobeam orientation; the presented unit vector is simplified via trigonometric relations. A visual representation of the dipoles and cavity vectors is provided in Fig. 4.

Substituting Eq. (8) into Eq. (7) yields

$$F_C = F_o \tfrac{1}{2} \sin^2 55° \,(1 + \sin 2\psi)\,, \tag{9}$$

$$F_D = F_o \tfrac{1}{2} \,(1 - \sin 2\psi)\,. \tag{10}$$

Taking the ratio eliminates F_o:

$$\frac{F_D}{F_C} = \frac{1}{\sin^2 55°} \frac{1 - \sin 2\psi}{1 + \sin 2\psi}. \tag{11}$$

Thus, the experimentally extracted Purcell factors provide a direct estimate of the cavity orientation ψ. Using the experimentally determined values for F_C and F_D, as reported in Sec. II B 3, Eq. (11) yields

$$\psi_{parallel} = 6.1 \pm 0.5°, \quad \psi_{angled} = 64.9 \pm 27.6°. \tag{12}$$

From these values, we can calculate the difference between the two angles $|\psi_{parallel} - \psi_{angled}| \approx 58.8°$, which exhibits a slight discrepancy from the expected 55°, as was lithographically defined; however, we note that the error for ψ_{angled} is considerable, given the large uncertainty in fitting the weakly enhanced D transition of the angled cavity.

Additionally, we can interpret $\psi_{parallel}$ as a global lithographic angular offset, $\delta\psi$. By allowing both $\delta\psi$ and the branching ratio η_{BR} to vary as free parameters, the two values can be jointly fitted. Performing this analysis yields $\delta\psi \approx 8.51°$ and $\eta_{BR} \approx 0.75 \pm 0.01$, the latter notably being consistent with literature values [6,18,22].

As expected, for ⟨100⟩ diamond, angling photonic crystal cavities such that $\psi = 45°$ would yield maximal overlap between cavity-mode polarization and the in-plane projection dipole moment of either the C or D transition. Although the D-transition dipole moment can nominally be perfectly aligned in plane for ⟨100⟩ diamond substrates, its smaller branching ratio renders optimizing coupling to the C transition favorable [15].

III. DISCUSSION

Our results highlight the importance of analyzing the lifetime reduction for both the C and D transitions. By explicitly modeling the shared excited-state spontaneous emission dynamics and accounting for the orthogonal polarizations of the C- and D-transition dipole moments,

we are able to extract not only the individual Purcell factors of each transition, but also the intrinsic C/D branching ratio of the SnV^-.

This contrasts with prior work, where Purcell factors are reported per SnV^- center and calculated by applying multiplicative correction factors without writing out an explicit, full treatment of the spontaneous emission dynamics of the system [12,17]. Furthermore, experimental determination of branching ratios previously relied on PL spectra or was determined through quasiresonant excitation [22,24]. Distinguishing the Purcell enhancements of the C and D transitions provides a more faithful description of the underlying physics, which indicates the optimal emitter-cavity alignment for maximizing subsequent spin-state readout fidelity.

The asymmetry in cavity coupling between orthogonal transitions further serves as a sensitive probe of dipole orientation relative to the cavity field, allowing us to extract the angular alignment of the fabricated devices with respect to the crystal axes. If the collective lithography offset from the main lattice vector is known independently, for example via x-ray diffraction measurements, the spontaneous emission equations for the C and D transitions in one cavity alone are sufficient to solve directly for both the branching ratio and Purcell factors. By investigating a second, angled cavity, we both validate our model and demonstrate the advantages of aligning the cavity-mode polarization as closely as possible to the dipole orientation of a specific transition. Indeed, if the angled cavity had been oriented 45° from the lattice vector rather than 55°, from our analysis, we would expect complete suppression of one transition and further increased enhancement of the other. By allowing for a controlled 10° of angular misalignment, we ensure that we are able to observe some degree of coupling between both C and D transitions of the emitter.

IV. CONCLUSION

In this manuscript, we report the fabrication of 1D photonic crystal cavity nanobeams from thin-film diamond membranes. We achieve quality factors of up to approximately 6000, and we observe up to tenfold PL enhancement from a select SnV^- when on resonance with the cavity mode. To accurately quantify our Purcell factors, we take time-resolved measurements and determine the optical-lifetime reduction of the emitter. Despite optically filtering to isolate the C transition in collection, we also observe lifetime reduction when the cavity is on resonance with the D transition of the same emitter.

From this picture, we construct a model describing the spontaneous emission dynamics of the system, with which we determine Purcell factors of $F_C = 9.2 \pm 0.2$ and $F_D = 8.9 \pm 0.1$ for the parallel cavity, and $F_C = 26.2 \pm 1.5$ and $F_D = 5.1 \pm 2.2$ for the angled cavity. Furthermore, by studying the cavity-emitter coupling behavior of these two devices we extract a C/D branching ratio of $\eta_{BR} \approx 0.75 \pm 0.01$ and a collective fabrication angular offset of $\delta\psi \approx 8.51°$.

Our Purcell factor can be further increased through fabrication optimization, such as improving feature fidelity and minimizing device sidewall angles in the etch process (Appendix A 3). Furthermore, cavity-SnV^- coupling can be improved through targeted and aligned implantation of Sn^{2+} into the cavity-mode volume [27]. The implantation density can be reduced for future devices to produce cavities with single color centers in the mode volume while also reducing general implantation damage of the material.

Our fabricated sample is compatible with microwave spin-driving experiments. By enhancing the SnV^- ZPL emission, the readout fidelity of SnV^- spins can be significantly enhanced [9,28]. Photon extraction can also be further improved by incorporating grating couplers or adiabatic tapers, which would enable color center addressing and photon collection in either transmission or reflection [18,29–31]. These developments would enable near-unity fidelity of single-shot readout of the electron spin in the SnV^-, paving the way for scalable quantum network nodes.

ACKNOWLEDGMENTS

This work was supported by the Department of Energy, Grant No. DE-SC0025295. This work was partially supported by Center for Integrated Nanotechnologies (CINT), a DOE Office of Science user facility jointly operated by Los Alamos and Sandia National Laboratories. This material is based upon work supported by the U.S. Department of Energy Office of Science National Quantum Information Science Research Centers as part of the Q-NEXT center. Q-NEXT supported a portion of fabrication expenditures, laboratory infrastructure, and student (H.C.K.) funding necessary for this project. We acknowledge the use of shared facilities of the UCSB Quantum Foundry through the Q-AMASE-i program (NSF DMR-1906325). H.C.K. acknowledges support by the Burt and Deedee McMurtry Stanford Graduate Fellowship (SGF). Work was performed in part in the nano@Stanford labs, which are supported by the National Science Foundation as part of the National Nanotechnology Coordinated Infrastructure under award ECCS-2026822.

DATA AVAILABILITY

The data that support the findings of this article are openly available [32].

APPENDIX A: FABRICATION OF THIN FILM AND DEVICE

1. Preparation of diamond thin film

The thin-film diamond material used for these experiments was prepared using the "smart cut" technique and subsequent membrane exfoliation, as reported in Ref. [20,21,33,34].

Electronic-grade, single-crystal diamond material was sourced from Element 6 and polished by Syntek to a miscut angle of 1°. The polishing-induced strained layer is removed via reactive-ion etching (RIE). A few micrometers is removed primarily by Ar/Cl etch chemistry, followed by a short (approximately 5 s) O_2 termination process to remove any Cl compounds on the surface. Helium ions (He^{2+}) were implanted into the diamond with an implantation energy of 150 keV at a fluence of 5×10^{16} ions/cm^2, and the chip was subsequently annealed at 850 °C in a high-vacuum chamber. The graphite layer formed from He^{2+} is approximately 100-nm thick and approximately 400 nm beneath the substrate surface [20].

Due to the high implantation energy and dosage, the material above the graphitization is rendered unsuitable for downstream color center formation and device fabrication. A new layer of diamond is thus grown homoepitaxially on the top surface using plasma-enhanced chemical vapor deposition. Detailed information on the growth procedure is reported in Ref. [35].

To form tin-vacancy centers, Sn^{2+} ions were implanted by a commercial vendor, Cutting Edge Ions, into the newly grown diamond layer with an implantation energy of 380 keV and a fluence of 2×10^{11} ions/cm^2. The Sn-implanted chip was high-vacuum annealed at 400 °C for 4 h, 800 °C for 4 h, and then 1200 °C for 2 h to promote color center formation. The sample was then triacid cleaned at 250 °C for 1 h to remove any surface graphitization that may have developed during the anneal. Lastly, a 90-min ultraviolet ozone treatment is used to oxygen-terminate the sample surface.

Membranes of size 200×200 μm^2 are patterned using photolithography and then released from the bulk using an electrochemical etch. The released membranes are then bonded, damaged-side up, to Si carrier pieces via the flowable oxide, hydrogen silsesquioxane (HSQ). Details on membrane exfoliation and transfer are outlined in Ref. [20]. The transferred membranes have a starting total thickness of 1 μm and are thinned to the final desired thickness of 180 nm using RIE. We show a schematic of the full membrane-preparation process in Fig. 5.

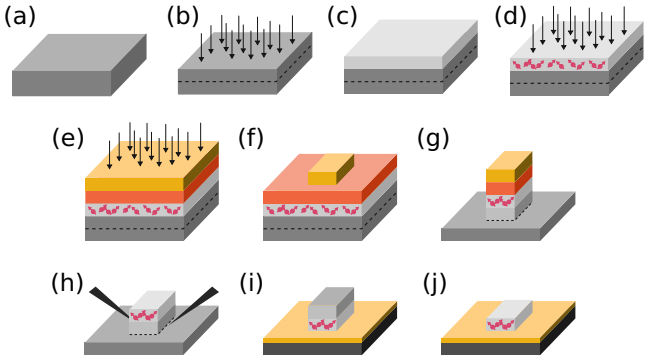

FIG. 5. Schematic of SnV^--implanted thin-film diamond preparation. (a) The process starts with a bulk electronic-grade diamond that is polished to a precise miscut angle. (b) The sample is then heavily implanted with He^{2+} ions to form a vertically localized graphitized layer, around 400 nm below the sample surface. (c) A pristine layer of single-crystalline diamond is grown over the implantation damaged layer. (d) Then, Sn^{2+} is implanted approximately 90 nm below the sample surface, and SnV^- centers are formed after high-temperature vacuum annealing. Any surface graphitization is removed via a triacid clean. (e) A silicon nitride (SiN) hard mask is then deposited via chemical vapor deposition and spun with photoresist. (f) Squares of 200×200 μm^2 are patterned by photolithography; these define the final size of each membrane. (g) The membranes are defined in the bulk diamond by an anisotropic RIE etch. (h) Individual membranes are then released via electrochemical etch, and (i) bonded to a Si carrier wafer with HSQ. (j) Finally, the film thickness is tuned to 180 nm via RIE.

2. Photonic crystal fabrication procedures

Fabrication of the photonic crystal begins with the prepared 180-nm thin-film membranes bonded to Si. An approximately 25-nm-thick Al_2O_3 hard mask is deposited via thermal atomic layer deposition (ALD). The sample is spin-coated with a positive e-beam resist (ZEP 520A)

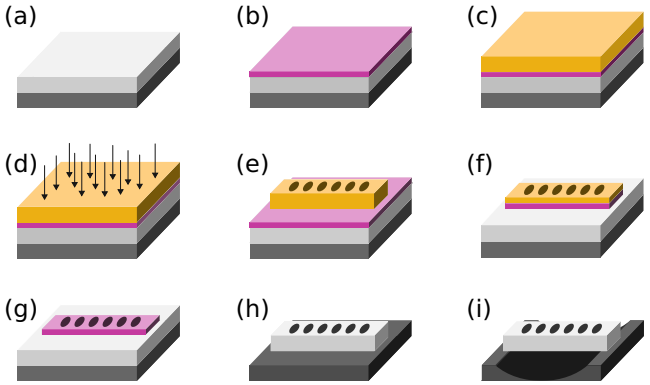

FIG. 6. Schematic of cavity fabrication procedure. (a) The starting material consists of thin-film diamond bonded to a Si handling wafer via HSQ. (b) A thin Al_2O_3 hard mask is deposited by ALD. (c) The sample is spun with ZEP and (d),(e) patterned via e-beam lithography. (f) The resist pattern is transferred into the hard mask by ICP-RIE etching. (g) Any remaining ZEP is then stripped, and (h) the pattern transferred into the diamond membrane. (i) Lastly, the devices are suspended by HF vapor and XeF_2 dry etching.

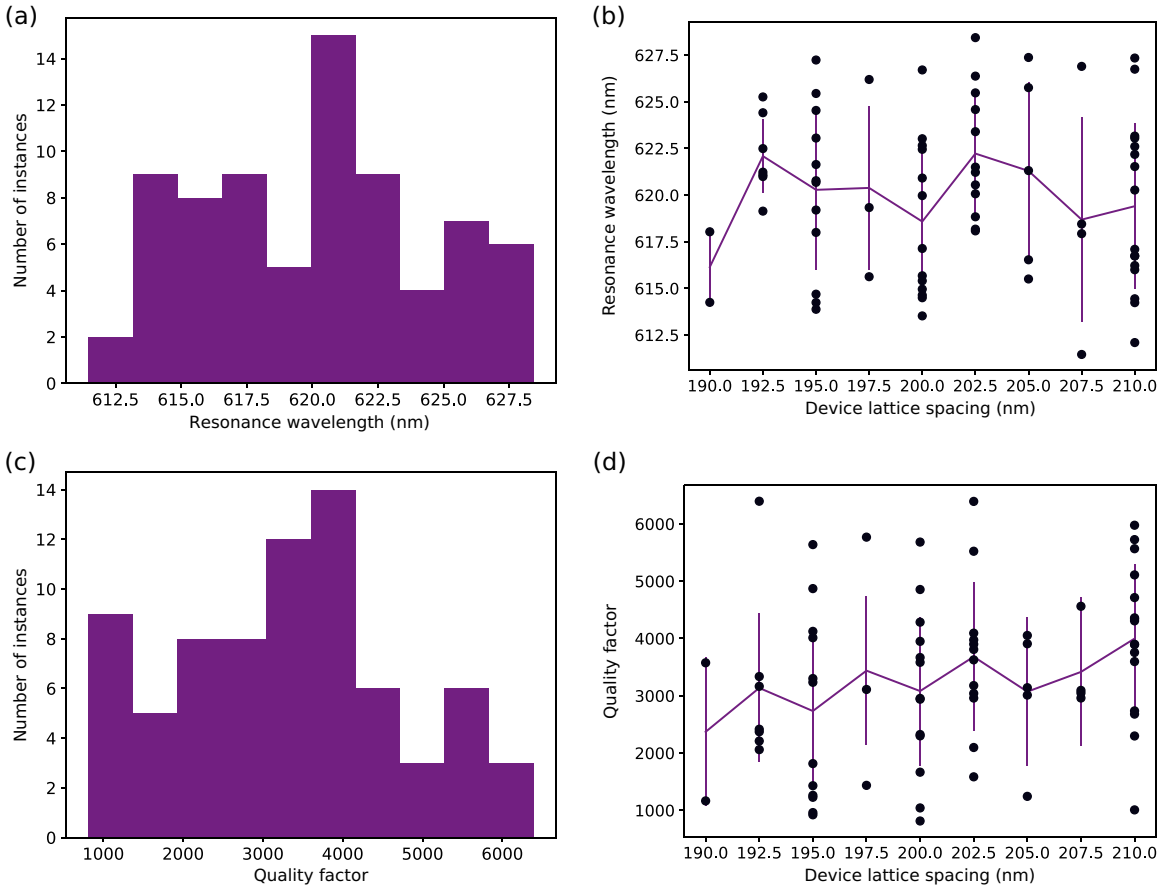

FIG. 7. Summary of cavity fabrication yield across the sample. (a) Histogram of resonance wavelengths for devices. Across all identified resonances, the average resonance wavelength is 620 ± 4 nm. (b) Resonance wavelengths of all devices, summarized by the device lattice spacing. The black markers are data points from individual devices, while the purple line and error bars indicate the average and standard deviation of resonance wavelengths for devices of specific lattice spacings. From simulations, we expect resonance wavelengths to redshift with increasing cavity lattice spacing. However, we do not observe a clear trend across our sample due to fabrication infidelities. (c) Histogram of quality factors for devices. Across all identified resonances, the average quality factor is 3335 ± 1428. (d) Quality factors of all devices, summarized by the device lattice spacing. The black markers are data points from individual devices, while the purple line and error bars indicate the average and standard deviation of quality factors for devices of specific lattice spacings. Quality factors are expected to remain roughly constant across all device designs. For our sample, the quality factor increases very slightly with lattice spacing.

and then the pattern is exposed via e-beam lithography. The resist pattern is transferred into the hard mask with a BCl_3 chemistry inductively coupled plasma (ICP) etch and subsequently transferred into the diamond via a Cl_2O_2/O_2 two-step cyclical ICP etch. The final devices are then released via HF and XeF_2 vapor dry etches. We show this process schematically in Fig. 6.

3. Yield and fidelity of cavity fabrication

To account for fabrication uncertainties, the cavity lattice spacing was swept from 180 to 210 nm, in steps of 2.5 nm, for a total of 13 device designs. All other design parameters (beam width, hole diameter, cavity lattice tapering factor) were kept constant. From finite-difference time-domain simulations, we expect resonance wavelengths to correspondingly vary from approximately 575 nm to approximately 684 nm, in steps of approximately 4 nm for each lattice-spacing step. In Fig. 7, we survey all devices across our sample to evaluate our fabrication yield and fidelity. Due to fabrication variation, we do not observe a clear trend between device lattice spacing and resonance wavelength. Quality factors seem to demonstrate a very slight increase with increased lattice spacings. We also note that we were unable to find any resonances for devices with the lowest four lattice spacings, ranging from 180 to 187.5 nm, most likely due to the over-etching of cavity holes.

We evaluated the fabrication fidelity in detail for the two devices of study in the manuscript. Using the GenISys PROSEM software package, we analyze the tapered lattice spacings of the cavity holes [Figs. 8(a) and 8(b)]. For

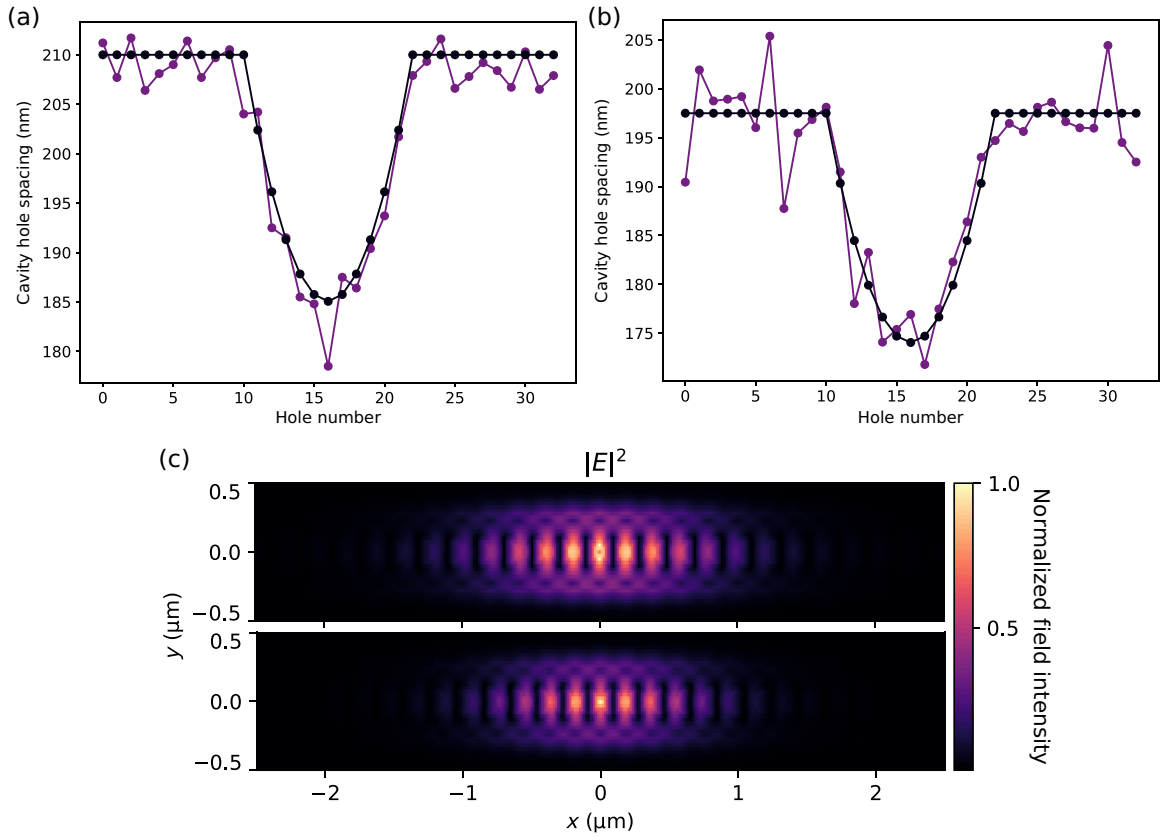

FIG. 8. Comparison of cavity lattice spacings. (a) Lattice-spacing deviations for the parallel device. On average, the cavity holes deviated by 2.013 ± 1 nm from their designed positions. The black markers indicate the designed air hole positions, and the purple the positions as measured via SEM. (b) Lattice-spacing deviations for the angled device. Cavity holes deviated by 2.796 ± 3 nm from their designed positions. The black markers indicate the designed air hole positions, and the purple the positions as measured via SEM. (c) Simulated normalized electric field inside the cavity region of the parallel device (top) and angled device (bottom).

the parallel device, we calculate a 2.013 ± 1 nm deviation from designed lattice spacings, and for the angled device, we calculate a 2.796 ± 3 nm deviation from designed spacings. Furthermore, we determine our device etch sidewall angle by fitting to both the top and bottom of the extracted beam-width sigmoid. For the parallel device, we determine top (bottom) beam widths of 292.6 ± 15 nm (358.6 ± 14 nm) and for the angled cavity, we extract 304.9 ± 2 nm (337.3 ± 13 nm). Given a consistent membrane thickness of 180 nm, we therefore determine sidewall angles of 10.389° and 5.143°, respectively, which are included in the simulations.

Cavities were initially designed around vertical (0°) sidewalls, and quality factors were optimized accordingly. Therefore, any sidewall angle resulting from fabrication serves as a primary source of quality-factor degradation as trapezoidal waveguide cross sections give rise to unwanted mixing between TE and TM modes. Furthermore, as the Sn^{2+} implantation depth was targeted as 90 nm below the membrane surface, the diamond thin films were tuned to 180 nm to best center the emitters in devices. However, the quality factors may be boosted by thinning the membrane slightly further (by approximately 20 nm) in future iterations.

APPENDIX B: CHARACTERIZATION SETUP

Here, we describe the optical setup used for device and emitter studies (Fig. 9). The optical setup consists of two separate access arms, referred to in the main manuscript as the PL and cross-polarized paths. Access between the two paths is controlled via a motorized mirror (Thorlabs MFF101).

The sample is housed in a Montana Instruments Cryostation s50 at 5 K and positioned via a triple Attocube piezo stack (X101/Z100). The sample is addressed with a 100-µm working distance, 100× magnification objective (Zeiss EC Epiplan-NEOFLUOR 100x/0.9), which is mounted in a heater cryo-objective housing. The 4f confocal scanning microscope is constructed from a pair

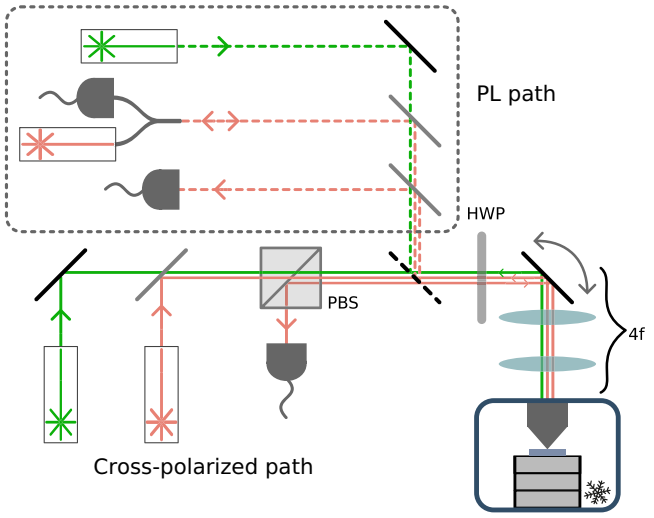

FIG. 9. Schematic of the measurement setup. The optical setup primarily consists of a home built, 4f confocal microscope with scanning enabled by a galvo mirror (4f). A HWP is inserted right before the galvo mirror, allowing for simultaneous polarization rotation of all excitation and collection paths. The optical setup incorporates two discrete optical paths, referred to in this manuscript as the PL and cross-polarized paths. Access to either of these paths is controlled via a flip mirror (dashed diagonal line). In the cross-polarized path, the excitation is horizontally polarized and the collection is vertically polarized, with the two paths mixed via a PBS. Green diode and broadband supercontinuum excitation are separately fed into the optical setup, with the two paths combined via a short-pass dichroic beamsplitter. For the PL path, collection is first split between green and red via a long-pass dichroic beamsplitter, and it is then further split between ZPL and PSB via a short-pass dichroic beamsplitter. When addressing emitters resonantly, the resonant laser is launched from the ZPL collection fiber coupler.

of 300-mm lenses (Thorlabs AC254-300-A) and a galvo mirror (Newport FSM-300-01). Polarization control is provided by the HWP (Thorlabs AHWP10M-600).

In the cross-polarized path, polarization filtering is provided by a polarizing beam splitter (Thorlabs CCM1-PBS251). In the horizontally polarized collection path, the free-space beam is coupled into a single mode (SM) fiber. In the horizontally polarized excitation arm, green and red wavelength splitting is achieved through a short-pass dichroic beamsplitter (Semrock TSP01-561). The red excitation arm provides either resonant laser (Toptica 1240 nm DL Pro, doubled via an ADVR frequency doubler) or broadband supercontinuum (SuperK EVO EUL-10) light, coupled through an SM fiber. A Thorlabs LP520-SF40 green diode laser is used for the above band excitation. A HWP (Thorlabs AHWP10M-600) and filter wheel are used to optimize and control power delivery, respectively.

In the PL path, we split green and red with via a long-pass dichroic beamsplitter (Semrock DMLP550). Subsequently, we split ZPL and PSB via a short-pass dichroic (Semrock FF625-SDi01). Pulsed 520-nm excitation is provided by a Thorlabs GSL52A laser. Either resonant excitation or signal can be launched or collected from the ZPL path.

The collected signal is either routed to single photon-counting modules (Excelitas SPCM-AQRH-24) or a hybrid spectrometer (Acton SpectraPro 2750 gratings and Andor iDus416 CCD). For lifetime measurements, the parallel device lifetimes are collected on a Picoquant Picoharp 300, while the angled device lifetimes are collected on a Swabian Timetagger Ultra. Due to different timing-resolution specifications, the parallel-device lifetimes are taken with 32-ps timing bins, and the angled-device lifetimes with 20-ps bins. During processing for the angled device, timing bins are further down-sampled to 40 ps. Pulse sequences are programmed and applied by a Swabian Pulse Streamer 8/2. Pulsing and attenuation of the resonant excitation laser is provided by a G&H, Fiber-Q 633-nm acousto-optic modulator (AOM).

Fiber fluorescence from the green excitation sources is cleaned up with Thorlabs FBH520-10 520/10-nm bandpass filters. Green scattering is further filtered from collection paths via Semrock BLP01-594R 594-nm long-pass filters. The ZPL signal is isolated through Semrock FBP01-620/14 620/14-nm bandpass filters. Filtering for isolating single SnV^- transition lines is achieved using a custom ordered Rapid Spectral Solutions 622/0.3-nm bandpass filter, designed to have approximately 5 nm of tuning range.

APPENDIX C: RESONANT COLOR CENTER ADDRESSING

Prior to patterning photonic devices, optical characterization was performed to verify formation of color centers in the thin-film material. Using 4f confocal microscopy, two-dimensional (2D) PL spatial maps were obtained using an above-resonant (green, 520 nm) diode laser and bright spots probed with spectroscopy [Fig. 10(a)]. From Fig. 10(b), the large density of SnV^-s formed is evident from the PL spectra. This high emitter density is also evident when resonantly addressing the SnV^- candidates. Within approximately 40 GHz of laser scanning range, we can address of the order of three to four color centers [Fig. 10(d)].

To study the spectral coherence of these color centers, we perform photoluminescence excitation (PLE) spectroscopy via the PL optical path. We excite the SnV^- with alternating pulsed green and red excitation. Single-photon counting module (SPCM) collection is gated with red excitation to reduce signal background. The full pulse sequence is 20 μs, with 4 μs of green excitation, 4 μs of offset, and 12 μs of red excitation and SPCM collection. Pulsing for the green diode is provided by direct modulation of the laser diode, while

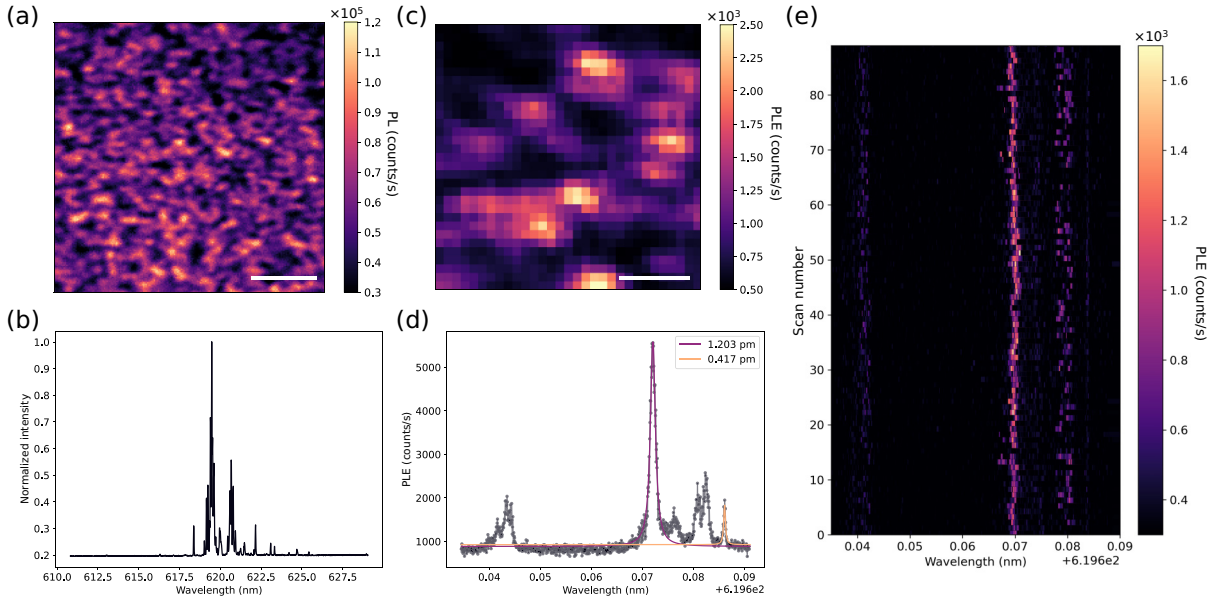

FIG. 10. Color center characterization in the thin film, before device fabrication. (a) PL confocal scan of the thin film before device fabrication. The density of bright spots indicates the larger number of SnV^-s formed during implantation. The scale bar indicates 3 μm. (b) Representative PL spectrum for a probed emitter cluster, demonstrating the SnV^- formation density. (c) PLE confocal scan. A full PLE scan is taken, and count rates are summed per pixel of the 2D spatial map. All emitters that appear are addressable within the laser scanning range of approximately 40 GHz. The scale bar indicates 1 μm. (d) Averaged PLE. Two representative transitions are fitted with a Lorentzian model to estimate the linewidths. The more prominent transition demonstrates a 1.236 pm or approximately 1 GHz linewidth. The other transition demonstrates a 0.417 pm or approximately 320 MHz linewidth. (e) PLE traces over 30 min. The stability of the PLE indicates prolonged SnV^- spectral coherence in the thin film.

pulsing for the red is provided by an AOM. The red laser is scanned across approximately 40 GHz with a frequency of 0.2 Hz. We are also able to identify SnV^- transitions with down to a linewidth of approximately 320 MHz, stable for around 30 min [Fig. 10(e)]; however, color centers of higher coherence in both bulk and thin-film diamond have been reported [14,36–38]. We attribute our measured linewidth to insufficient optimization of PLE experimental parameters, lack of an exhaustive survey of emitters, and the high Sn^{2+} implantation density.

After device fabrication, we first attempt PLE spectroscopy for the emitter of study in the parallel device. Although the PLE is consistent over approximately 30 min, the emitter demonstrates significant linewidth broadening, with an averaged linewidth of 15.382 pm [Figs. 11(a) and 11(d)]. We also probe a secondary emitter in the device that is much more weakly coupled to the cavity mode. This emitter instead demonstrates an averaged linewidth of 1.368 pm, and the PLE signal is similarly stable over approximately 30 min. The further linewidth broadening of the emitters in fabricated devices likely stemmed from the proximity of etched surfaces. To mitigate these effects, inspiration can be taken from efforts to improve near-surface NV coherence via surface passivation or chemical termination [39,40].

APPENDIX D: EXTENDED METHODS AND DATA

1. Secondary emitter in the angled cavity mode

In this section, we discuss the behavior of the second emitter in the angled cavity mode. Due to the bandwidth of the tunable optical filter (approximately 0.3 nm), a small contribution from a second emitter is collected during lifetime measurements for the angled cavity. This contribution is visible when a PL spectrum is taken from the optically filtered collection spot with long integration times [Fig. 12(a)].

When the C (D) transition is on resonance, the secondary emitter demonstrates a reduced lifetime of 8.01 ± 0.07 ns (6.66 ± 0.20 ns). By fitting the data to the sum of four Lorentzians and extracting the relevant amplitudes, we determine amplitude ratios of $\zeta_C = 1.02 \pm 0.16$ and $\zeta_D = 1.97 \pm 0.28$. Given that the D transition demonstrates greater lifetime reduction than the C transition, we conclude that this secondary emitter is orthogonal in orientation to the other two SnV^-s of study. Using literature values for η_{DW} and η_{BR}, we determine Purcell factors of $F_C = 1.1 \pm 0.4$ and $F_D = 8.8 \pm 2.2$, for the C and D transitions, respectively.

As performed in Sec. II B 4, we can attempt to solve for η_{BR} and $\delta\psi$, now taking into account this secondary emitter. From Fig. 12(c), we see that the three trendlines fail to fully intersect. This discrepancy is likely due to increased

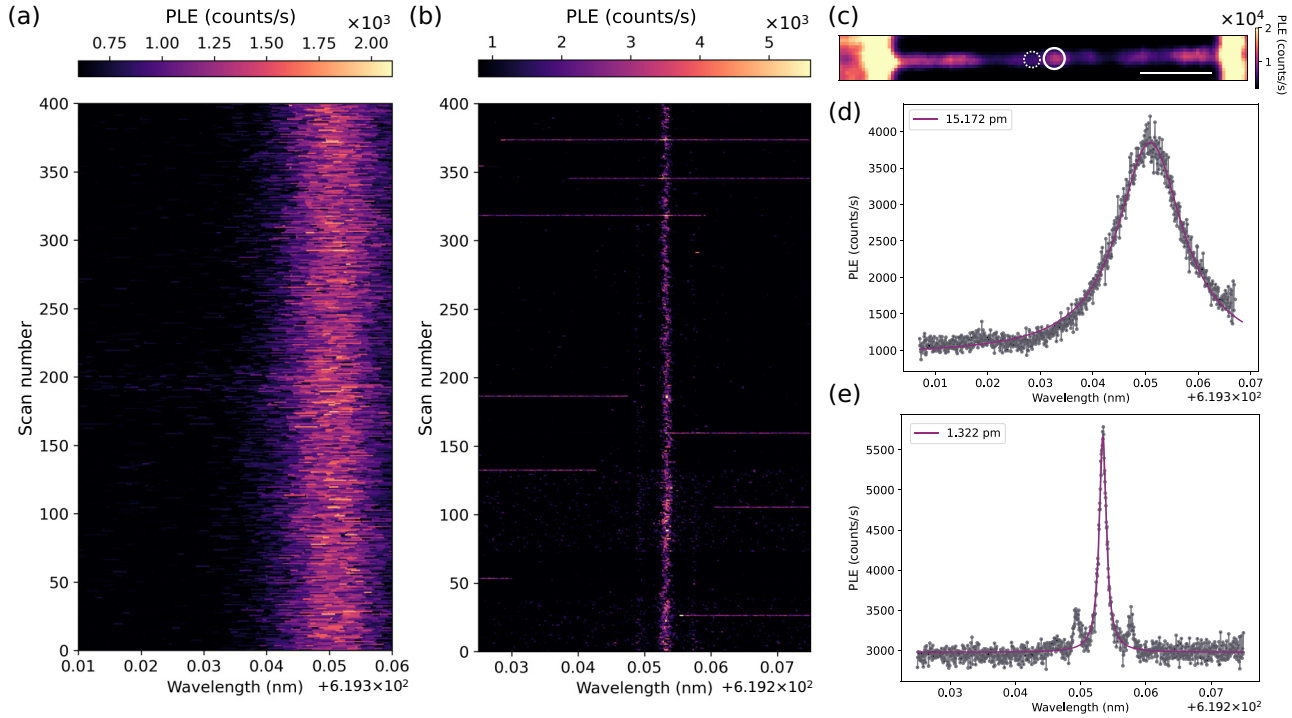

FIG. 11. Resonant color center addressing in fabricated devices. (a) PLE traces for approximately 30 min on the color center of focus in the parallel device. (b) PLE traces for approximately 30 min for a secondary emitter in the parallel device. (c) PLE confocal scan of the parallel device. The main emitter studied in this manuscript is indicated by the solid circle, while the dashed circle indicates the secondary emitter of study. (d) Averaged PLE of the traces from (a). A Lorentzian fit yields a linewidth of 15.382 pm. (e) Averaged PLE of the traces from (b). A Lorentzian fit yields a linewidth of 1.386 pm. We note that the side lobes of the main PLE peak feature were due to laser instability and multimodedness.

fitting errors, stemming from further reduced SNR per lifetime measurement for this more weakly coupled emitter. Therefore, we instead minimize the averaged pairwise differences between all trend lines, identifying the optimal value $\eta_{\mathrm{BR}} \approx 0.75 \pm 0.06$, consistent with that determined in Sec. II B 3.

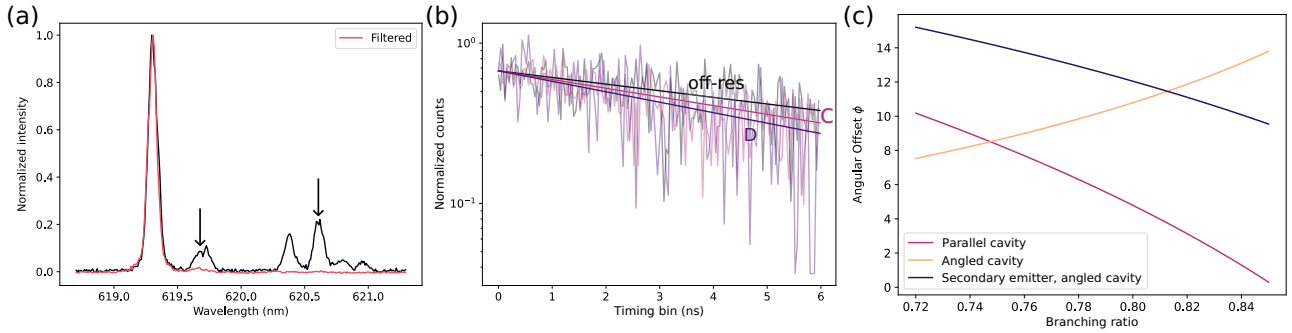

FIG. 12. Lifetime reduction of secondary emitter. (a) Filtered and unfiltered PL spectra of the collection spot for the angled device. Both are normalized to show the degree of suppression of other transitions by the tunable filter. The arrows indicate the estimated C and D transitions of the second emitter. In the filtered spectrum, it is evident that a small contribution from the secondary C transition remains. (b) Lifetime reduction when the secondary emitter is on or off resonance. The C transition demonstrates a reduced lifetime of 8.01 ± 0.07 ns, and D demonstrates a reduced lifetime of 6.66 ± 0.20 ns. The off-resonance lifetime is 10.51 ± 0.20 ns. (c) Solution for Purcell analysis for three emitters. Although the three functions fail to intersect, minimizing the average difference yields $\eta_{\mathrm{BR}} = 0.75 \pm 0.06$, consistent with the value calculated in Sec. II B 3. We also similarly determine the global lithographic angular offset to be $\delta\psi \approx 8.51^{\circ}$.

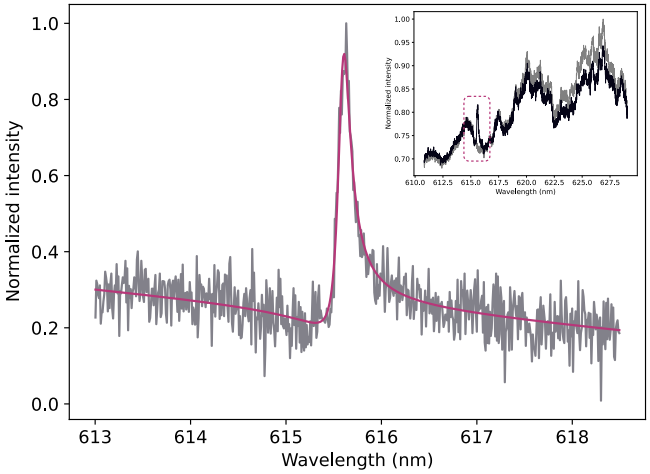

FIG. 13. Angled-cavity quality-factor characterization. The full broadband reflectivity spectra for the resonance and background are shown in the inset. The fitted region is indicated by the dashed line. As with the parallel device, the resonance is fitted to a Fano model. In the inset, the background is represented by the grey trace, and the resonance signal by the black trace.

2. Angled cavity and PL characterization

When measured in cross-polarized reflectivity, the angled device yields a quality factor of 3942, determined through a Fano fit on a background-corrected broadband spectrum (Fig. 13). In Fig. 14, we also present a PL confocal scan of the angled device of interest. Similar to the parallel cavity, the high implantation dose resulted in a cluster of two to three emitters coupled to the cavity mode. The most strongly enhanced transition demonstrates an approximately 2.25-fold PL enhancement when on resonance with the cavity (Fig. 14). We note that this figure illustrates the necessity of lifetime-reduction measurements for rigorously determining Purcell factors in a cavity QED system.

3. Quality-factor measurement

To probe for cavity resonances via cross-polarized reflectivity, we first generated a 2D map via PL confocal scanning, and we then visually estimated the coordinates of the center of the photonic crystal cavity nanobeam. The galvo mirror was then used to perform a small spatial sweep around this estimated center (Fig. 15). A broadband reflectivity spectrum was collected at each spatial location, and spatially sensitive, narrow features were flagged as resonances. A spectrum that was located spatially adjacent to a location exhibiting a resonant feature was used for background subtraction.

The cross-polarized reflectivity spectra are highly sensitive to small changes in HWP orientation, which was adjusted and optimized manually. This sensitivity, in conjunction with noise that arises from the reflection measurement (e.g., coupling of the excitation to free-space modes above the light line), causes the resonances collected via this measurement technique to be Fano rather than Lorentzian in lineshape. This contributes an additional source of uncertainty in the extracted quality factors given the increased number of fitting parameters in the Fano model. To evaluate the degree of uncertainty in our quality-factor determination, we compared the quality factors determined from cross-polarized reflectivity with those from PL excitation (Fig. 16), wherein the cavity modes are excited via fluorescence from the color centers. When probing the quality factors via PL on the same devices reported in the main text, we determine a quality factor of 6745 ± 342 for the parallel device and 4533 ± 154 for the

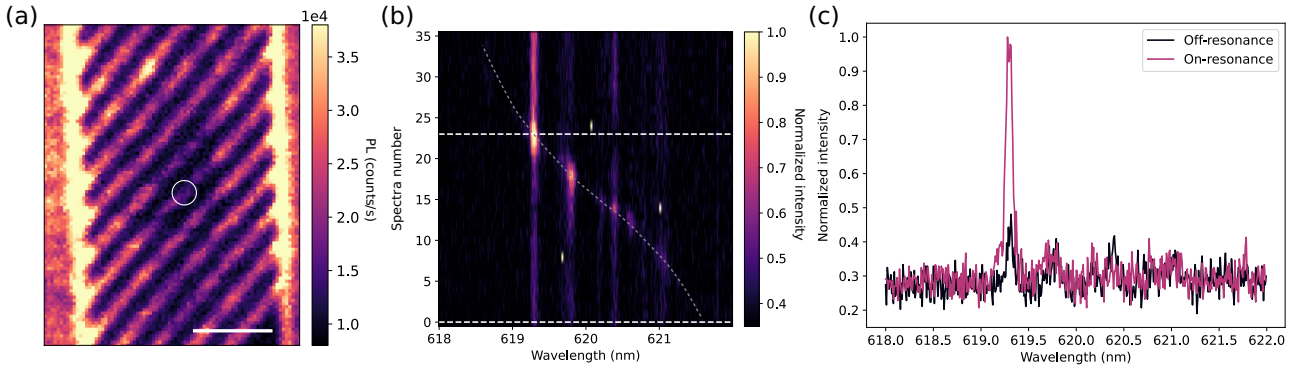

FIG. 14. Angled-cavity PL confocal scan and cavity enhancement. (a) PL confocal scan of the angled device studied in this manuscript. The emitter cluster of focus is indicated by the white circle. The scale bar indicates 3 μm. (b) PL enhancement of the SnV^-s located in the angled-device cavity mode. The spectra for the transition of interest on and off resonance are indicated by the white dashed lines. The grey dashed line is a guide for the eye, indicating the cavity resonance wavelength. (c) PL spectra of the two transitions of interest. From comparing the transition amplitude on and off resonance, we estimate a 2.5-fold PL enhancement from gas tuning.

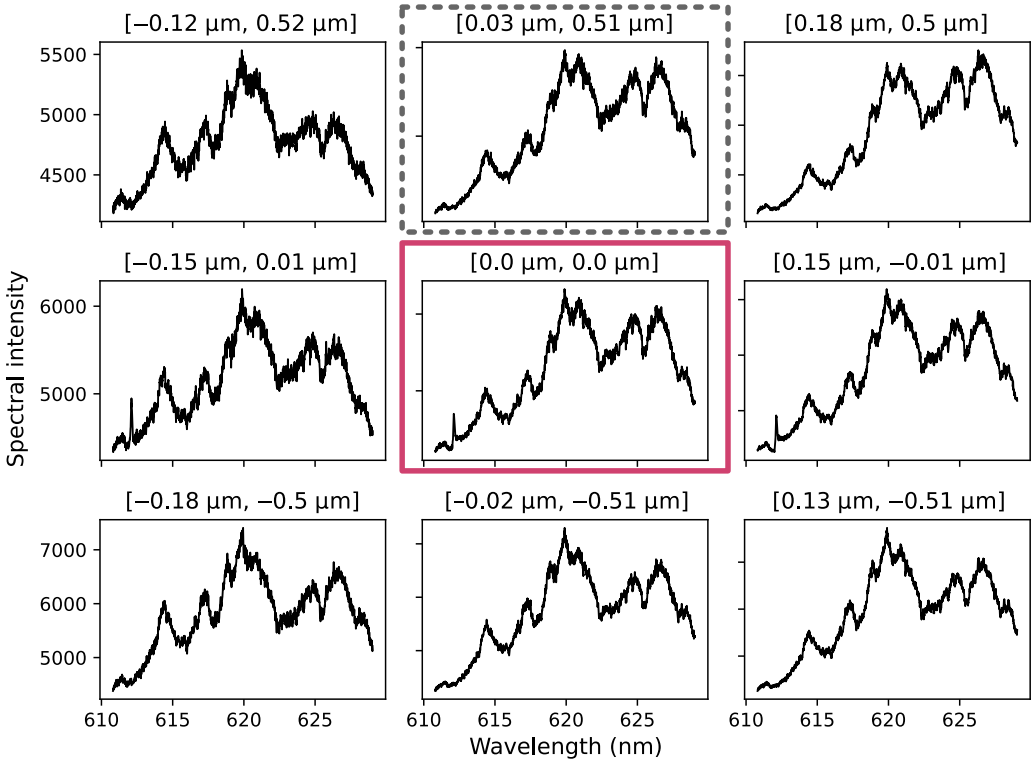

FIG. 15. Example array of spectra from a spatial location sweep to identify the position of resonance for the parallel device presented in the main text. The spectrum used to measure the resonance is indicated by the pink box, and that used for background subtraction is shown by the gray dashed box. Each spectrum is labeled with its spatial offset from the one used to determine the cavity quality factor.

angled device. Both of these Q values were extracted from a Lorentzian model, which provides an appropriate fit for the resonance lineshapes measured via PL excitation. As expected, the quality factors derived from the Lorentzian-shaped resonances seen via PL excitation are higher than the quality factors extracted from the Fano-shaped reflectivity spectra. The Q values extracted from the reflectivity measurements are thus taken to be a lower bound.

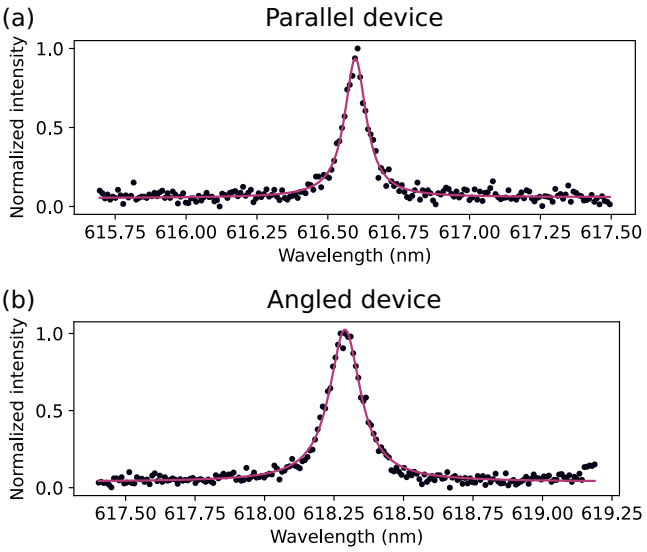

FIG. 16. Comparison of resonance fitting via PL spectra for the (a) parallel and (b) angled devices. On this occasion, for the parallel (angled) device, we measure a quality factor of 6745 ± 342 (4533 ± 154). From these fitted values, we conclude that the quality factors determined via cross-polarized reflectivity serve as lower-bound estimates.

4. Cavity-mode polarization dependence

To verify that the nanobeam cavity modes are linearly polarized, we measure the angular dependence of the

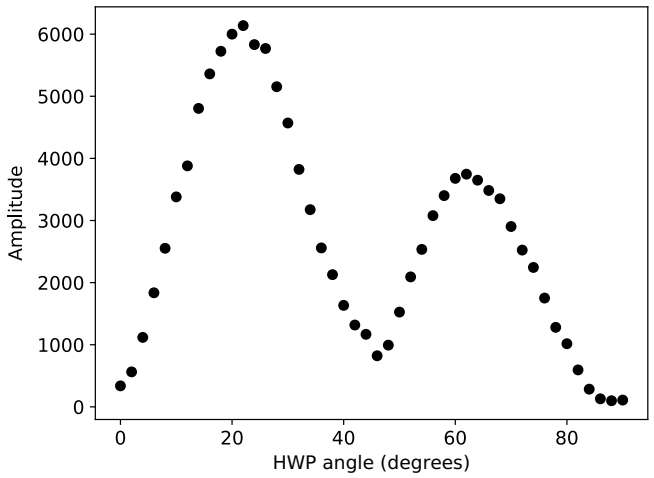

FIG. 17. Angular dependence of cavity reflectivity amplitude. The periodicity of the oscillatory behavior is approximately 45°, indicating a linearly polarized mode.

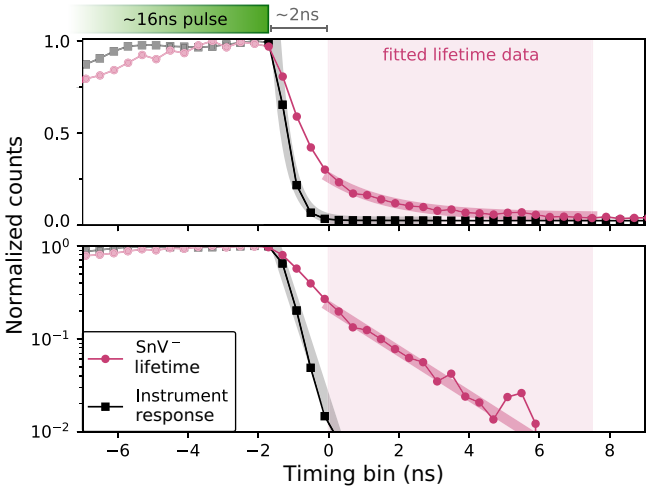

FIG. 18. IRF of the optical setup. Color centers are excited with 16-ns pulses at a repetition rate of 3.3 MHz. The IRF is fitted to a single exponential model, yielding a fall time of approximately 370 ps. Therefore, 2 ns of each lifetime trace is truncated, and the remaining data, shaded in pink, are fitted to single exponential models. The most reduced lifetime trace, corresponding to 1.079 ns, is displayed in both linear (top) and logarithmic (bottom) scales to verify negligible effects from the IRF.

reflectivity amplitude by rotating the HWP. The angular dependence demonstrates sinusoidal behavior with a periodicity of approximately 45°, indicating a linearly polarized mode (Fig. 17) [41]. The amplitude modulation of the sinusoidal trend is likely due to slight shifts in beam positioning introduced by HWP rotation.

5. Lifetime processing and instrument response function

We characterize our optical setup's instrument response function (IRF) via the PL path. We focus the pulsed green laser on the sample surface, attenuate the power to prevent detector saturation, and then remove the long-pass collection filter. The fall time of the IRF is then fitted with a single exponential decay, yielding a fall time of approximately 370 ps, slightly above the 300 ps jitter expected of the SPCM detectors. To take this into account, the first approximately 2 ns of each lifetime trace is therefore truncated and the remainder is fitted to a single exponential decay (Fig. 18).

[1] H. J. Kimble, The quantum internet, Nature **453**, 1023 (2008).
[2] D. D. Awschalom, R. Hanson, J. Wrachtrup, and B. B. Zhou, Quantum technologies with optically interfaced solid-state spins, Nat. Photonics **12**, 516 (2018).
[3] M. Atatüre, D. Englund, N. Vamivakas, S.-Y. Lee, and J. Wrachtrup, Material platforms for spin-based photonic quantum technologies, Nat. Rev. Mater. **3**, 38 (2018).
[4] M. Pompili, S. L. N. Hermans, S. Baier, H. K. Beukers, P. C. Humphreys, R. N. Schouten, R. F. L. Vermeulen, M. J. Tiggelman, L. dos Santos Martins, B. Dirkse *et al.*, Realization of a multinode quantum network of remote solid-state qubits, Science **372**, 259 (2021).
[5] H. Bernien, B. Hensen, W. Pfaff, G. Koolstra, M. S. Blok, L. Robledo, T. H. Taminiau, M. Markham, D. J. Twitchen, L. Childress *et al.*, Heralded entanglement between solid-state qubits separated by three metres, Nature **497**, 86 (2013).
[6] G. Thiering and A. Gali, Ab initio magneto-optical spectrum of group-IV vacancy color centers in diamond, Phys. Rev. X **8**, 021063 (2018).
[7] C. M. Knaut, A. Suleymanzade, Y.-C. Wei, D. R. Assumpcao, P.-J. Stas, Y. Q. Huan, B. Machielse, E. N. Knall, M. Sutula, G. Baranes *et al.*, Entanglement of nanophotonic quantum memory nodes in a telecom network, Nature **629**, 573 (2024).
[8] T. Iwasaki, Y. Miyamoto, T. Taniguchi, P. Siyushev, M. H. Metsch, F. Jelezko, and M. Hatano, Tin-vacancy quantum emitters in diamond, Phys. Rev. Lett. **119**, 253601 (2017).
[9] E. I. Rosenthal, C. P. Anderson, H. C. Kleidermacher, A. J. Stein, H. Lee, J. Grzesik, G. Scuri, A. E. Rugar, D. Riedel, S. Aghaeimeibodi *et al.*, Microwave spin control of a tin-vacancy qubit in diamond, Phys. Rev. X **13**, 031022 (2023).
[10] E. I. Rosenthal, S. Biswas, G. Scuri, H. Lee, A. J. Stein, H. C. Kleidermacher, J. Grzesik, A. E. Rugar, S. Aghaeimeibodi, D. Riedel *et al.*, Single-shot readout and weak measurement of a tin-vacancy qubit in diamond, Phys. Rev. X **14**, 041008 (2024).
[11] A. E. Rugar, C. Dory, S. Aghaeimeibodi, H. Lu, S. Sun, S. D. Mishra, Z.-X. Shen, N. A. Melosh, and J. Vučković, Narrow-linewidth tin-vacancy centers in a diamond waveguide, ACS Photonics **7**, 2356 (2020).
[12] A. E. Rugar, S. Aghaeimeibodi, D. Riedel, C. Dory, H. Lu, P. J. McQuade, Z.-X. Shen, N. A. Melosh, and J. Vučković, Quantum photonic interface for tin-vacancy centers in diamond, Phys. Rev. X **11**, 031021 (2021).
[13] R. Debroux, C. P. Michaels, C. M. Purser, N. Wan, M. E. Trusheim, J. Arjona Martínez, R. A. Parker, A. M. Stramma, K. C. Chen, L. de Santis, E. M. Alexeev, A. C. Ferrari, D. Englund, D. A. Gangloff, and M. Atatüre, Quantum control of the tin-vacancy spin qubit in diamond, Phys. Rev. X **11**, 041041 (2021).
[14] X. Guo *et al.*, Microwave-based quantum control and coherence protection of tin-vacancy spin qubits in a strain-tuned diamond-membrane heterostructure, Phys. Rev. X **13**, 041037 (2023).
[15] N. Codreanu, T. Turan, D. B. Rodriguez, M. Pasini, L. de Santis, M. Ruf, C. F. Primavera, L. G. C. Wienhoven, C. E. Smulders, S. Gröblacher, and R. Hanson, Above-unity coherent cooperativity of tin-vacancy centers in diamond photonic crystal cavities, arXiv:2511.13375 [quant-ph].
[16] I. Karapatzakis, J. Resch, M. Schrodin, P. Fuchs, M. Kieschnick, J. Heupel, L. Kussi, C. Sürgers, C. Popov, J. Meijer, C. Becher, W. Wernsdorfer, and D. Hunger, Microwave control of the tin-vacancy spin qubit in diamond with a superconducting waveguide, Phys. Rev. X **14**, 031036 (2024).

[17] K. Kuruma, B. Pingault, C. Chia, D. Renaud, P. Hoffmann, S. Iwamoto, C. Ronning, and M. Lončar, Coupling of a single tin-vacancy center to a photonic crystal cavity in diamond, Appl. Phys. Lett. **118**, 230601 (2021).

[18] M. Pasini, N. Codreanu, T. Turan, A. Riera Moral, C. F. Primavera, L. De Santis, H. K. C. Beukers, J. M. Brevoord, C. Waas, J. Borregaard, and R. Hanson, Nonlinear quantum photonics with a tin-vacancy center coupled to a one-dimensional diamond waveguide, Phys. Rev. Lett. **133**, 023603 (2024).

[19] S. W. Ding, M. Haas, X. Guo, K. Kuruma, C. Jin, Z. Li, D. D. Awschalom, N. Delegan, F. J. Heremans, A. A. High, and M. Loncar, High-Q cavity interface for color centers in thin film diamond, Nat. Commun. **15**, 6358 (2024).

[20] H. Oh, V. Dharod, C. Padgett, L. B. Hughes, J. Venkatraman, S. Parthasarathy, E. Osipova, I. Hedgepeth, J. V. Cady, L. Basso *et al.*, A spin-embedded diamond optomechanical resonator with mechanical quality factor exceeding one million, Optica **13**, 485 (2026).

[21] X. Guo, N. Delegan, J. C. Karsch, Z. Li, T. Liu, R. Shreiner, A. Butcher, D. D. Awschalom, F. J. Heremans, and A. A. High, Tunable and transferable diamond membranes for integrated quantum technologies, Nano Lett. **21**, 10392 (2021).

[22] A. E. Rugar, C. Dory, S. Sun, and J. Vučković, Characterization of optical and spin properties of single tin-vacancy centers in diamond nanopillars, Phys. Rev. B **99**, 205417 (2019).

[23] A. Faraon, P. E. Barclay, C. Santori, K.-M. C. Fu, and R. G. Beausoleil, Resonant enhancement of the zero-phonon emission from a colour centre in a diamond cavity, Nat. Photonics **5**, 301 (2011).

[24] J. L. Zhang, S. Sun, M. J. Burek, C. Dory, Y.-K. Tzeng, K. A. Fischer, Y. Kelaita, K. G. Lagoudakis, M. Radulaski, Z.-X. Shen, N. A. Melosh, S. Chu, M. Lončar, and J. Vučković, Strongly cavity-enhanced spontaneous emission from silicon-vacancy centers in diamond, Nano Lett. **18**, 1360 (2018).

[25] J. Görlitz, D. Herrmann, G. Thiering, P. Fuchs, M. Gandil, T. Iwasaki, T. Taniguchi, M. Kieschnick, J. Meijer, M. Hatano, A. Gali, and C. Becher, Spectroscopic investigations of negatively charged tin-vacancy centres in diamond, New J. Phys. **22**, 013048 (2020).

[26] C. Hepp, T. Müller, V. Waselowski, J. N. Becker, B. Pingault, H. Sternschulte, D. Steinmüller-Nethl, A. Gali, J. R. Maze, M. Atatüre, and C. Becher, Electronic structure of the silicon vacancy color center in diamond, Phys. Rev. Lett. **112**, 036405 (2014).

[27] A. Sipahigil, R. E. Evans, D. D. Sukachev, M. J. Burek, J. Borregaard, M. K. Bhaskar, C. T. Nguyen, J. L. Pacheco, H. A. Atikian, C. Meuwly, R. M. Camacho, F. Jelezko, E. Bielejec, H. Park, M. Lončar, and M. D. Lukin, An integrated diamond nanophotonics platform for quantum-optical networks, Science **354**, 847 (2016).

[28] R. E. Evans, M. K. Bhaskar, D. D. Sukachev, C. T. Nguyen, A. Sipahigil, M. J. Burek, B. Machielse, G. H. Zhang, A. S. Zibrov, E. Bielejec, H. Park, M. Lončar, and M. D. Lukin, Photon-mediated interactions between quantum emitters in a diamond nanocavity, Science **362**, 662 (2018).

[29] M. J. Burek, C. Meuwly, R. E. Evans, M. K. Bhaskar, A. Sipahigil, S. Meesala, B. Machielse, D. D. Sukachev, C. T. Nguyen, J. L. Pacheco, E. Bielejec, M. D. Lukin, and M. Lončar, Fiber-coupled diamond quantum nanophotonic interface, Phys. Rev. Appl. **8**, 024026 (2017).

[30] R. A. Parker, J. Arjona Martínez, K. C. Chen, A. M. Stramma, I. B. Harris, C. P. Michaels, M. E. Trusheim, M. H. Appel, C. M. Martin, W. G. Roth, D. Englund, and M. Atatüre, A diamond nanophotonic interface with an optically accessible deterministic electronuclear spin register, Nat. Photonics **18**, 156 (2024).

[31] C. T. Nguyen, D. D. Sukachev, M. K. Bhaskar, B. Machielse, D. S. Levonian, E. N. Knall, P. Stroganov, R. Riedinger, H. Park, M. Lončar, and M. D. Lukin, Quantum network nodes based on diamond qubits with an efficient nanophotonic interface, Phys. Rev. Lett. **123**, 183602 (2019).

[32] Data available at: http://bit.ly/3NpTZOM.

[33] J. C. Lee, A. P. Magyar, D. O. Bracher, I. Aharonovich, and E. L. Hu, Fabrication of thin diamond membranes for photonic applications, Diam. Relat. Mater. **33**, 45 (2013).

[34] Y. Li, F. A. Gerritsma, S. Kurdi, N. Codreanu, S. Gröblacher, R. Hanson, R. Norte, and T. van der Sar, A fiber-coupled scanning magnetometer with nitrogen-vacancy spins in a diamond nanobeam, ACS Photonics **10**, 1859 (2023).

[35] L. B. Hughes, Z. Zhang, C. Jin, S. A. Meynell, B. Ye, W. Wu, Z. Wang, E. J. Davis, T. E. Mates, N. Y. Yao *et al.*, Two-dimensional spin systems in PECVD-grown diamond with tunable density and long coherence for enhanced quantum sensing and simulation, APL Mater. **11**, 021101 (2023).

[36] M. E. Trusheim *et al.*, Transform-limited photons from a coherent tin-vacancy spin in diamond, Phys. Rev. Lett. **124**, 023602 (2020).

[37] J. M. Brevoord, L. D. Santis, T. Yamamoto, M. Pasini, N. Codreanu, T. Turan, H. K. Beukers, C. Waas, and R. Hanson, Heralded initialization of charge state and optical-transition frequency of diamond tin-vacancy centers, Phys. Rev. Appl. **21**, 054047 (2024).

[38] K. Ikeda, Y. Chen, P. Wang, Y. Miyamoto, T. Taniguchi, S. Onoda, M. Hatano, and T. Iwasaki, Charge state transition of spectrally stabilized tin-vacancy centers in diamond, ACS Photonics **12**, 2972 (2025).

[39] S. Sangtawesin, B. L. Dwyer, S. Srinivasan, J. J. Allred, L. V. H. Rodgers, K. De Greve, A. Stacey, N. Dontschuk, K. M. O'Donnell, D. Hu, D. A. Evans, C. Jaye, D. A. Fischer, M. L. Markham, D. J. Twitchen, H. Park, M. D. Lukin, and N. P. de Leon, Origins of diamond surface noise probed by correlating single-spin measurements with surface spectroscopy, Phys. Rev. X **9**, 031052 (2019).

[40] R. Kumar, S. Mahajan, F. Donaldson, S. Dhomkar, H. J. Lancaster, C. Kalha, A. A. Riaz, Y. Zhu, C. A. Howard, A. Regoutz, and J. J. L. Morton, Stability of near-surface nitrogen vacancy centers using dielectric surface passivation, ACS Photonics **11**, 1244 (2024).

[41] Y. Gong and J. Vučković, Photonic crystal cavities in silicon dioxide, Appl. Phys. Lett. **96**, 031107 (2010).